**Chemistry of Metals and Alloys**

*Chem. Met. Alloys* 7 (2014) 74-84
Ivan Franko National University of Lviv
www.chemetal-journal.org

# Superconducting non-centrosymmetric boride $Mg_{10}Ir_{19}B_{16}$: crystal structure and chemical bonding

Anastasia M. ALEKSEEVA[1,2,3]*, Andreas LEITHE-JASPER[1], Yurii PROTS[1], Walter SCHNELLE[1], Alim ORMECI[1], Evgeny V. ANTIPOV[2], Yuri GRIN[1]

[1] *Max-Planck-Institut für Chemische Physik fester Stoffe, Nöthnitzer Str. 40, 01187 Dresden, Germany*
[2] *Department of Chemistry, Lomonosov Moscow State University, 119991 Moscow, Russia*
[3] *MPG-MSU Partner Group, Department of Chemistry, Lomonosov Moscow State University, 119991 Moscow, Russia*
* *Corresponding author. Tel.: +7-495-9395244; fax: +7-495-9394788; e-mail: alekseevaam@gmail.com*

Dedicated to Evgen I. Gladyshevskii (1924-2012)

Received January 27, 2014; accepted June 26, 2014; available on-line November 10, 2014

**A single-phase sample of $Mg_{10}Ir_{19}B_{16}$ was prepared from the elements by high-temperature treatment in sealed Ta containers. The crystal structure of $Mg_{10}Ir_{19}B_{16}$ (space group $I\bar{4}3m$, $a$ = 10.5657(2) Å, $Z$ = 2) was solved and refined using X-ray single crystal diffraction data. The chemical composition was confirmed by WDXS analysis. The absence of any significant homogeneity range was proven *via* lattice parameter determinations for samples of different nominal compositions. Electronic structure calculations and chemical bonding analysis by the ELI/ED approach revealed that the basis of the $Mg_{10}Ir_{19}B_{16}$ structure is formed by a 3D anionic framework of covalent polar B–Ir bonds. Mainly ionic interactions were found between the Mg cations and the anionic framework, supported by additional dative Ir–Mg bonding.**

**Superconducting boride / Crystal structure / Chemical bonding**

## Introduction

The discovery of the superconducting properties of magnesium diboride $MgB_2$ with $T_c$ = 39 K [1] motivated numerous studies on related compounds [2]. The layered crystal structure containing flat boron layers was considered to be a key to new boride superconductors [3]. However, attempts to synthesize new boride superconductors, by modification of the $MgB_2$ crystal structure, were mainly unsuccessful [4]. More evident results were achieved in the re-investigation of the superconducting properties of binary transition metal borides with significantly lower $T_c$ [3]. The discovery of the new superconducting boride $Mg_{10}Ir_{19}B_{16}$ [5] (together with $Li_2(Pt,Pd)_3B$ [6]) represents a rather rare example of successful preparation of new boride superconducting compounds. In spite of the relatively low transition temperature of $T_c$ = 4.5 K, $Mg_{10}Ir_{19}B_{16}$ has attracted great interest, due to its unique crystal structure. The non-centrosymmetric structure of $Mg_{10}Ir_{19}B_{16}$ has no relations to the basic structure types of complex transition-metal borides. It is very difficult to visualize and to describe this crystal structure using traditional geometric approaches. The problem of the interpretation of the $Mg_{10}Ir_{19}B_{16}$ structure was hampered by the absence of reliable structure data and chemical analyses. In the earliest publication [5], the crystal structure of $Mg_{10}Ir_{19}B_{16}$ was solved from electron diffraction data. Taking into account the low contribution of boron to the overall scattering factor (especially in such Ir-rich structure), together with the absence of single-phase material, variability of the chemical composition was postulated [5]. This led to debates on the homogeneity range of $Mg_{10}Ir_{19}B_{16}$ in the following publications [6-8]. The first structure determination of $Mg_{10}Ir_{19}B_{16}$ was performed using a non-single-phase polycrystalline powder sample in a combined experimental and calculation procedure [9]. In spite of the careful and detailed investigation of the physical properties [10-12], results of crystal structure refinements on single-crystal diffraction data, or of investigations of the homogeneity range, have not yet been published. It seems as if the complexity of the crystal structure (cell volume of more than 1000 Å$^3$) on the one hand, and the problems connected with the interpretation of the crystal structure on the other hand, have led to the absence of reliable investigations of the electronic structure and chemical bonding for $Mg_{10}Ir_{19}B_{16}$.

In the present work we report new data concerning the compound $Mg_{10}Ir_{19}B_{16}$: preparation of single-phase material and a study of the homogeneity range, structure solution from single-crystal XRD data and chemical bonding analysis. We believe these data will be helpful for the further understanding of the crystal structure and interpretation of the superconducting properties.

## Experimental

*1. Synthesis and characterization*

Samples with the nominal composition $Mg_{10}Ir_{19}B_{16}$ were prepared starting from powders of magnesium (Alfa Aesar, 99.8 %), iridium (Chempur, 99.9 %) and crystalline boron (Alfa Aesar, 99.999 %). The oxygen and carbon contents in the initial materials were determined by the carrier gas hot extraction method (combined infra-red and heat-conduction detector TC 436 DR/5, LECO, USA). The oxygen content was found to be lower than the detection limit (≤ 0.038 mass%) in the iridium and crystalline boron powders, and 0.14(3) mass% in the magnesium powder. The carbon content was found to be lower than the detection limit (≤ 0.03 mass%) in the iridium and crystalline boron powders, and 0.12(2) mass% in the magnesium powder.

All operations of the synthesis were performed in a glove box under argon atmosphere (content of $O_2$ and $H_2O$ ≤ 0.1 ppm). Taking into account the low reactivity of crystalline boron ($B_{cr}$) a fraction of $B_{cr}$ with a particle size ≤ 20 μm was separated by sieving and intimately mixed with appropriate amounts of magnesium and iridium powders in an agate mortar, pressed into pellets and sealed into tantalum containers (diameter 8 mm, length 25 mm). The tantalum containers were sealed into evacuated silica ampoules and annealed at 850-1100 ºC for 3-7 days with one intermediate re-grinding in argon atmosphere. The ampoules were finally cooled in the furnace to room temperature.

Phase identification and lattice parameter determination were performed using room-temperature X-ray powder diffraction data (image plate Guinier camera Huber G670, Cu $K_{\alpha 1}$ radiation, $\lambda$ = 1.540598 Å) with $LaB_6$ as internal standard ($a$ = 4.15690(5) Å). The program package WinXPOW [13] was used for data processing and refinement of the unit-cell parameters.

Metallographic investigation was performed on polished samples with an optical microscope Zeiss Axiotec 100, equipped with polarizer and analyzer. The whole setup, including the polishing system, was placed in an argon-filled glove box, in order to protect the materials against reaction with air and moisture [14]. The local chemical composition was investigated by EDXS with a Philips XL30 SEM (tungsten cathode, 30 kV) with EDAX attachment (S-UTW-Si(Li) detector). Because of the high absorption of Ir ($\mu_m$ = 3098 cm$^2$ g$^{-1}$) for Mg-$K_\alpha$ radiation (1.253 keV) [15]) only a semi-quantitative analysis was feasible by EDXS. A more precise investigation of the chemical composition was carried out by WDXS with an external standard. The binary phase MgIr was synthesized and analytically characterized to use as standard material for Mg and Ir determination. WDXS measurements were performed with a CAMECA SX100 EPMA device; 15 kV excitation conditions. A TLAP crystal/FPC detector was used for registration of the Mg-$K_\alpha$ signal, a 25 kV/LiF(200)/SC detector for Ir-$L_\alpha$ data collection.

For the investigation of the potential homogeneity range, the dependence of the lattice parameter on the initial sample composition was studied. For this purpose, samples with initial compositions $Mg_{22.2\pm x}Ir_{42.2\pm y}B_{35.6\pm z}$, *i.e.* varying around the stoichiometric composition (22.2 at.% Mg, 42.2 at.% Ir, 35.6 at.% B), were prepared.

*2. Single-crystal X-ray diffraction*

A single crystal of $Mg_{10}Ir_{19}B_{16}$, suitable for X-ray data collection, was selected from a sample with nominal composition $MgIr_3B_8$, annealed at 1250 ºC for 14 days (heated over 50 h, cooled by water quenching). The crystal structure was determined using single-crystal X-ray diffraction data collected with a Rigaku AFC 7 (Mercury CCD) diffraction system. The collected data were processed using the WinCSD program package [16]. Details of the data collection and crystallographic information are given in Tables 1-4.

*3. Physical properties measurements*

Magnetization was measured in a SQUID magnetometer (MPMS-XL7, Quantum Design). The electrical resistivity was determined by four-contact low-frequency ac measurements (PPMS, Quantum Design). Thin wires were attached to the sample using silver-filled epoxy glue.

*4. Calculation procedures*

Electronic structure calculations of $Mg_{10}Ir_{19}B_{16}$ were carried out with the lattice parameters and atomic positions from the crystal structure refinement on single-crystal X-ray diffraction data (Tables 1-2). The TB-LMTO-ASA program package [17] was employed, using the Barth-Hedin exchange potential [18] for the LDA calculations. The radial scalar-relativistic Dirac equation was solved to obtain the partial waves. Because the calculation within the atomic sphere approximation (ASA) includes corrections for the neglect of interstitial regions and partial waves of higher order [19], addition of empty spheres was not necessary. The following radii of the atomic spheres were used for the calculations: $r$(Mg1) = 1.876 Å, $r$(Mg2) = 1.854 Å, $r$(Ir1) = 1.489 Å, $r$(Ir2) = 1.351 Å, $r$(Ir3) = 1.415 Å, $r$(B1) = 1.090 Å, and $r$(B2) = 1.022 Å. For each calculation, a basis set containing Mg(3*s*,3*p*),

**Table 1** Crystallographic information for $Mg_{10}Ir_{19}B_{16}$.

| | |
|---|---|
| Chemical composition | $Mg_{10}Ir_{19}B_{16}$ |
| Formula mass | 4068.206 |
| Crystal shape | irregular |
| Crystal system | cubic |
| Space group | $I\bar{4}3m$ |
| $a$, Å | 10.5657(2) [a] |
| $V$, Å$^3$ | 1179.49(2) |
| $Z$ | 2 |
| Radiation $\lambda$, Å | Mo $K_\alpha$, 0.71073 |
| Max. $\sin\theta/\lambda$ | 0.778 |
| Calculated density, g/cm$^3$ | 11.450(3) |
| Absorption coefficient, cm$^{-1}$ | 1133.67 |
| Measured reflections | 6663 |
| Symmetry-independent reflections | 260 |
| $R_{eq}$ | 0.064 |
| Reflections used for refinement | 254 |
| Number of parameters refined | 23 |
| Extinction coefficient | 0.00019(7) |
| $R(F)$, $R(F^2)$ for all data | 0.022, 0.033 |
| Largest diff. peak, $e^-$/Å$^3$ | 3.00 |

[a] from X-ray powder diffraction data.

**Table 2** Atomic coordinates and isotropic displacement parameters for $Mg_{10}Ir_{19}B_{16}$.

| Atom | Site | $x/a$ | $y/b$ | $z/c$ | $B_{eq/iso}$, Å$^2$ [a] |
|---|---|---|---|---|---|
| Mg1 | 8*c* | 0.3390(9) | *x* | *x* | 1.34(2) |
| Mg2 | 12*e* | 0.3514(2) | 0 | 0 | 2.0(2) |
| Ir1 | 12*d* | ¼ | ½ | 0 | 0.44(1) |
| Ir2 | 2*a* | 0 | 0 | 0 | 0.52(2) |
| Ir3 | 24*g* | 0.25294(5) | *x* | 0.07145(6) | 0.44(1) |
| B1 | 24*g* | 0.1634(2) | *x* | 0.4110(2) | 0.4(2) |
| B2 | 8*c* | 0.109(3) | *x* | *x* | 1.3(7) |

[a] $B_{eq} = 1/3[a^{*2}a^2B_{11} + b^{*2}b^2B_{22} + c^{*2}c^2B_{33} + 2aba^*b^*(\cos\gamma)B_{12} + 2aca^*c^*(\cos\beta)B_{13} + 2bcb^*c^*(\cos\alpha)B_{23}]$.

**Table 3** Anisotropic displacement parameters [a,b] (Å$^2$) for $Mg_{10}Ir_{19}B_{16}$.

| Atom | $B_{11}$ | $B_{22}$ | $B_{33}$ | $B_{12}$ | $B_{13}$ | $B_{23}$ |
|---|---|---|---|---|---|---|
| Mg1 | 1.3(2) | $B_{11}$ | $B_{11}$ | 0 | 0 | 0 |
| Mg2 | 3.2(6) | 1.4(3) | $B_{22}$ | 0 | 0 | 0 |
| Ir1 | 0.36(2) | $B_{11}$ | 0.59(3) | 0 | 0 | 0 |
| Ir2 | 0.52(2) | $B_{11}$ | $B_{11}$ | 0 | 0 | 0 |
| Ir3 | 0.43(1) | 0.45(2) | $B_{11}$ | 0.11(1) | 0.10(2) | 0 |

[a] The displacement parameters of the boron atoms were refined isotropically.
[b] The anisotropic displacement parameters are defined as: $\exp[-1/4(a^{*2}h^2B_{11} + b^{*2}k^2B_{22} + c^{*2}l^2B_{33} + 2a^*b^*hkB_{12} + 2a^*c^*hlB_{13} + 2b^*c^*klB_{23})]$.

Ir(6*s*,6*p*,5*d*) and B(2*s*,2*p*) orbitals was employed with Mg(3*d*), Ir(4*f*) and B(3*d*) functions being downfolded.

The electron localizability indicator (ELI, $\Upsilon$) was evaluated in the ELI-D representation according to [20-22] with an ELI-D module from the program package TB-LMTO-ASA [17]. Topological analysis of the electron density, *i.e.* estimation of the shapes, volumes and charges of the atoms after Bader (quantum theory of atoms in molecules, QTAIM [23]), and of the electron localizability indicator, *i.e.* localization of the ELI maxima as fingerprints of the direct atomic interactions, was performed with the program DGrid [24].

**Table 4** Selected interatomic distances in $Mg_{10}Ir_{19}B_{16}$.

| Atoms | Distance, Å | Atoms | Distance, Å |
|---|---|---|---|
| Mg1 − 3B1 | 2.67(2) | Ir3 − 1B1 | 2.10(2) |
| 3Ir3 | 2.826(9) | 2B1 | 2.15(2) |
| 3Ir3 | 3.025(9) | 1B2 | 2.19(3) |
| 3B2 | 3.03(3) | 2Ir3 | 2.7122(8) |
| 1Ir2 | 3.040(9) | 2Ir1 | 2.7177(6) |
| Mg2 − 2B1 | 2.52(2) | 1Mg1 | 2.826(9) |
| 4Ir3 | 2.966(6) | 2Mg2 | 2.966(6) |
| 2B2 | 3.04(3) | 1Mg1 | 3.025(9) |
| 2Ir1 | 3.073(8) | B1 − 1Ir3 | 2.10(2) |
| Ir1 − 4B1 | 2.17(2) | 2Ir3 | 2.15(2) |
| 4Ir3 | 2.7177(6) | 2Ir1 | 2.17(2) |
| 4Mg2 | 3.073(8) | 1Mg2 | 2.52(2) |
| Ir2 − 4B2 | 1.99(3) | 1Mg1 | 2.67(2) |
| 4Mg1 | 3.040(9) | B2 − 1Ir2 | 1.99(3) |
| | | 3Ir3 | 2.19(3) |
| | | 2Mg3 | 2.792(2) |
| | | 3Mg1 | 3.03(3) |
| | | 3Mg2 | 3.04(3) |

## Results and discussion

*1. Synthesis and composition*

The existence of the $Mg_{10}Ir_{19}B_{16}$ compound in the iridium-rich part of the ternary Mg–Ir–B system was confirmed. The X-ray powder diffraction data was indexed with a body-centered cubic lattice and a unit cell parameter of $a = 10.5657(2)$ Å. The stoichiometry of the phase was firstly determined by single crystal X-ray diffraction (see below). Optimization of the synthetic conditions (composition of the initial mixture, temperature and duration of annealing and cooling procedures) was performed in order to prepare a single-phase sample of $Mg_{10}Ir_{19}B_{16}$. Annealing of an element mixture with starting composition $Mg_{11}Ir_{19}B_{16}$ at 1100 ºC for 7 days (60 h heating, cooling over 48 h to 40 ºC) yielded a $Mg_{10}Ir_{19}B_{16}$ sample with negligible amount of impurity phase ($I_{max}$(impurity phase) / $I_{max}(Mg_{10}Ir_{19}B_{16}) \approx 0.02$) (Fig. 1).[1]

Metallographic and WDXS investigation of the sample showed the presence of the main phase with an Ir/Mg atomic ratio of 1.8(1), together with a small amount of impurity phase with higher iridium content. The Ir/Mg ratio obtained for the main phase is in good agreement with the $Mg_{10}Ir_{19}B_{16}$ single crystal diffraction data (Ir/Mg = 1.9). The composition of the impurity phase could not be precisely determined due to the very small crystalline size.

The results of the determination of the lattice parameters in samples with different initial composition around $Mg_{10}Ir_{19}B_{16}$ are presented in Table 5. No detectable changes of the lattice parameter were found. Thus, we consider $Mg_{10}Ir_{19}B_{16}$ as a phase with constant composition.

*2. Solution and refinement of the crystal structure*

The crystal structure of $Mg_{10}Ir_{19}B_{16}$ was determined using single-crystal X-ray diffraction data. The reflection condition *hkl*, $h + k + l = 2n$ and Laue class *m*-3*m* were found from intensity statistics. Only three possible space groups are in agreement with the extinction conditions found: $Im\bar{3}m$, $I\bar{4}3m$, and $I432$. Structure solution in the space group of highest symmetry ($Im\bar{3}m$) led to systematic splitting into half-occupied atomic positions, thus indicating possible symmetry reduction. The positions of the Ir atoms were found by direct methods in space group $I\bar{4}3m$. The magnesium and boron positions were obtained from Fourier and difference Fourier maps. The refinement of the crystal structure was performed with an anisotropic approach for the atomic displacement parameters (ADP) of the Mg and Ir atoms, whereas the displacement parameters of the boron atoms were refined as isotropic (Tables 2-4). As expected from the atomic mass, the magnesium positions have much larger ADP than the iridium atoms. The two Mg sites differ in their anisotropy

[1] The reflections corresponding to this impurity phase were also observed for the other samples obtained during the investigation in the ternary system Mg–Ir–B. They were indexed in orthorhombic unit cell with lattice parameters $a = 9.3618(4)$ Å, $b = 22.518(1)$ Å, $c = 5.3622(1)$ Å. From the X-ray powder diffraction data reflections conditions for the impurity phase were found to be $h + k$, $h + l$, $k + l = 2n$ for the *hkl* reflections ($h00$: $h = 4n$, $0k0$: $k = 4n$, $00l$: $l = 4n$) that corresponded to space group *Fddd*. No similar structures are known among ternary borides of platinum metals with magnesium or related binary compounds [25]. The study of the crystal structure of this phase is ongoing.

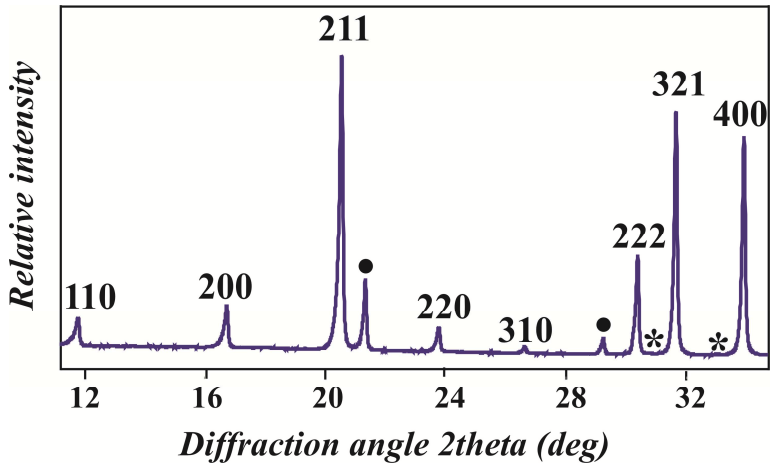


**Fig. 1** X-ray powder diffraction pattern of a sample with nominal composition $Mg_{10}Ir_{19}B_{16}$. The reflections of the main phase $Mg_{10}Ir_{19}B_{16}$ are indexed. $LaB_6$ (•) was added as an internal reference. The reflections of the impurity phase are marked (*).

**Table 5** Lattice parameters of the $Mg_{10}Ir_{19}B_{16}$ phase in multi-phase samples of different compositions.

| Nominal composition | at.% | | | *a*, Å |
|---|---|---|---|---|
| | Mg | Ir | B | |
| $Mg_{16}Ir_{17.5}B_{16.5}$ | 32 | 35 | 33 | 10.5658(1) |
| $Mg_{11.5}Ir_{20.5}B_{18}$ | 23 | 41 | 36 | 10.5657(1) |
| $Mg_{11}Ir_{20}B_{18.5}$ | 22 | 41 | 37 | 10.5655(1) |
| $Mg_{11}Ir_{19}B_{16}$ | 24 | 41 | 35 | 10.5657(2) |
| $Mg_{10.5}Ir_{19}B_{16}$ | 23 | 42 | 35 | 10.5658(1) |

whereas the displacement of Mg1 is clearly isotropic for symmetrical reasons, $B_{11}$ for the Mg2 position is significantly larger than $B_{22}$ and $B_{33}$. Refinement of the Mg1 and Mg2 site occupancies with fixed displacement parameters ($B_{iso}$ = 0.5 Å$^2$) resulted in the value 0.99(1). The difference Fourier map did not reveal residual electron density peaks higher than 3 e$^-$/Å$^3$. The anisotropy of the Mg2 position may be a consequence of its atomic environment. The differences between the isotropic APDs of the B1 and B2 atoms can also arise from the anisotropy of the atomic displacement due to the different coordination environment of these positions within the B-Ir framework.

*3. Description of the crystal structure*

The crystal structure of $Mg_{10}Ir_{19}B_{16}$, representing a new structure type, is not characteristic for ternary borides of magnesium and platinum metals. The first coordination sphere of both boron sites is formed by iridium. All boron and iridium atoms in $Mg_{10}Ir_{19}B_{16}$ are involved in a three-dimensional system of B–Ir contacts shorter than 2.2 Å (compare with the sum of covalent radii of iridium and boron, 2.25 Å [26]). Atom B1 is surrounded by five Ir atoms forming a strongly distorted tetragonal pyramid $[(B1)(Ir3)_3(Ir1)_2]$, inside which one contact, B1–Ir3, is significantly shorter than the others (Fig. 2a). Three tetragonal pyramids are condensed by edges in a block. These blocks are interconnected by sharing common vertices into a 3D framework with square channels along the four-fold axis (Fig. 2b). The magnesium atoms Mg1 and Mg2 are located at short distances to B1 atoms (2.52 Å and 2.67 Å, respectively). Previous investigations of chemical bonding in ternary magnesium borides [27,28] allows interpreting such short Mg–B contacts as a result of charge transfer from the magnesium substructure to the boron–platinum metal substructure. The second boron atom – B2 – is located inside a tetrahedron $[(B2)(Ir3)_3(Ir2)]$ where one of the faces is a regular triangle $(Ir3)_3$, and the polyhedron is elongated along a three-fold axis (Fig. 2c). The $[(B2)(Ir3)_3(Ir2)]$ tetrahedra are interconnected through one common vertex, Ir2, in blocks of four. These blocks are isolated from each other and situated at the positions of site symmetry $\bar{4}3m$ (Fig. 2d). One interatomic contact inside each tetrahedra, B2–Ir2 (1.99 Å), is significantly shorter than the three others (2.19 Å). B2 atoms from four neighboring $[(B2)(Ir3)_3(Ir2)]$ tetrahedra form a regular tetrahedron $[(Ir2)(B2)_4]$,

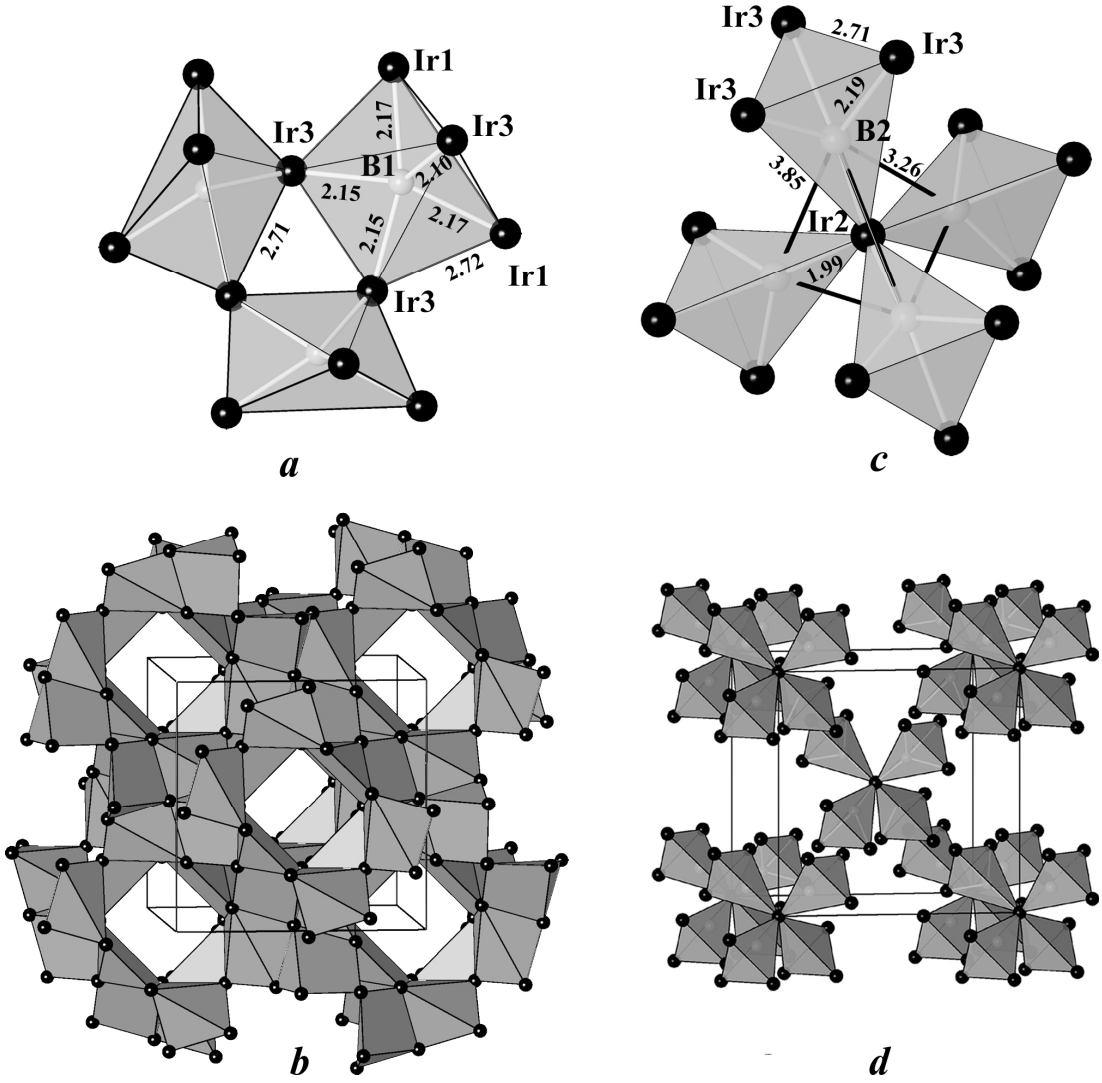


**Fig. 2** Crystal structure of $Mg_{10}Ir_{19}B_{16}$: (*a*) block of tetragonal pyramids $[(B1)(Ir3)_3(Ir1)_2]$; (*b*) framework of tetragonal pyramids $[(B1)(Ir3)_3(Ir1)_2]$; (*c*) block of tetrahedra $[(B2)(Ir3)_3(Ir2)]$ with $[(Ir2)(B2)_4]$ tetrahedron edges marked; (*d*) arrangement of $[(B2)(Ir3)_3(Ir2)]$ tetrahedra within the unit cell. The interatomic distances are given in Å.

centered at the Ir2 position (Fig. 2c). The coordination polyhedra of the B1 and B2 atoms are connected with each other by common edges and vertices into a 3D framework, the cavities of which are occupied by magnesium atoms. The Mg2 atoms are located inside relatively large cavities (between blocks of $[(B2)(Ir3)_3(Ir2)]$ tetrahedra along the four-fold axes), whereas the cavities hosting the Mg1 atoms are smaller.

*4. Electronic structure and chemical bonding*

In order to understand the relation between the electronic and crystal structures, first the electronic density of states (DOS) was calculated (Fig. 3). The results of our TB-LMTO-ASA calculations agree well with those obtained by the Korringa-Kohn-Rostocker technique [29]. Interestingly, the total DOS and its partial atomic contributions are very similar to the values obtained for some other superconducting compounds of transition metals with *p* elements, *e.g.* $RE_2Fe_3Si_5$, where *RE* is a rare-earth metal [30]. The DOS below the Fermi level consists of two well separated regions. The low-energy range ($E < -8$ eV) is mainly composed of *s* states of boron and *d* states of iridium with minor participation of Mg(*s*) and Ir(*s*), which may indicate a bonding interaction between iridium and boron. This conclusion is in agreement with the existence of a 3D system of short B–Ir contacts in the crystal structure (Fig. 2, Table 4), The DOS region below the Fermi level ($-7.5$ eV $< E < E_F$) can be subdivided into three parts. The density of states between –7.5 eV and –6 eV is mainly formed by Ir(*d*) and Mg(*s*) states, with small admixture of Ir(*s*), B(*s*) and B(*p*) contributions. This suggests Mg–Ir interactions. The middle part of the DOS ($-6$ eV $< E <$ –2 eV) mainly consists of B(*p*) and Ir(*d*) contributions,

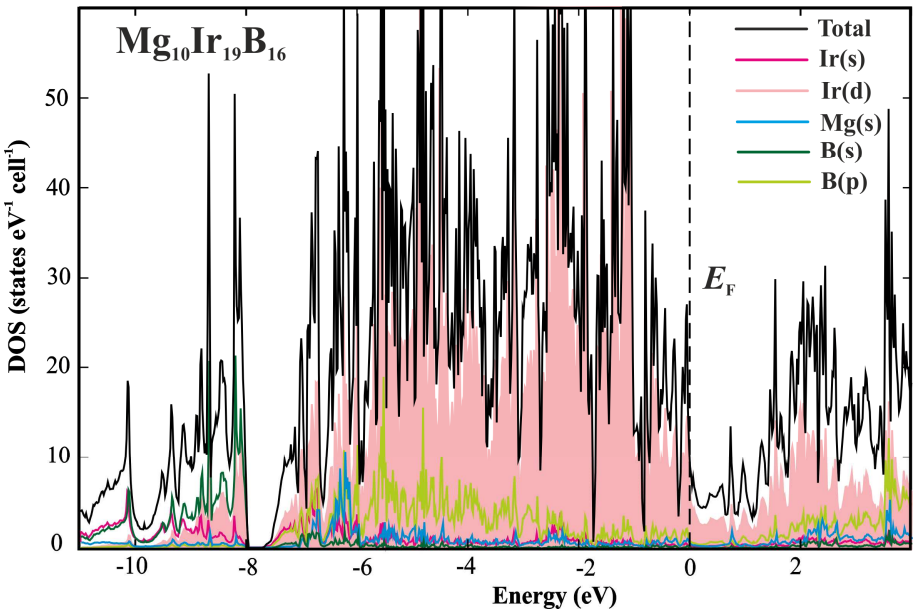


**Fig. 3** Total electron density of states of $Mg_{10}Ir_{19}B_{16}$ and partial atomic contributions.

in agreement with direct B–Ir interactions. Just below the Fermi level, the DOS is dominated by Ir(*d*) states, similarly to the $RE_2Fe_3Si_5$ superconductors where the DOS below $E_F$ is formed by Fe(*d*) states, this situation being considered as one of the fingerprints for possible superconducting behavior [30]. Contrarily to the latter group of superconductors, a pseudo gap is observed in $Mg_{10}Ir_{19}B_{16}$, just above the Fermi level, indicating a more covalent character of the atomic interactions in this compound, in comparison with the silicides mentioned above.

Further insight into the organization of the crystal structure of $Mg_{10}Ir_{19}B_{16}$ was obtained analyzing the atomic interactions in real space within the electron localizability approach [24]. Based on the electronegativity values of the components ($EN$(Ir) > $EN$(B) > $EN$(Mg), *e.g.* 2.20, 2.04 and 1.31 after Pauling, or 5.40, 4.29 and 3.75 on the absolute scale [26]), the interaction between the B–Ir substructure and the embedded Mg atoms may be expected to be ionic. In this case the Mg atoms transfer their valence electrons to the anionic B–Ir framework. Because of the small electronegativity difference between iridium and boron, their common presence in the anionic substructure is obvious. This expectation is supported by the atomic charges calculated according to the quantum theory of atoms in molecules (QTAIM [23]). The shapes of the QTAIM atoms (atomic basins), together with the effective charges, in $Mg_{10}Ir_{19}B_{16}$, are shown in Fig. 4. The atomic basins of Mg have shapes deviating from spherical, which might be expected assuming their role as cations (*cf.* Sr in $Sr_8Al_6Si_{40}$ [31] or Mg in $Mg_{1-x}B_2$ [32]). The basins of Ir and B resemble the coordination of these atoms in the crystal structure, having tetrahedron- or trigonal-bipyramid-like shapes. Integration of the electron density within the atomic basins yields practically identical effective charges of around +1.5 for the two magnesium sites. These values are very close to those recently observed for Mg in $Mg_3Rh_5B_3$ and $Mg_{11}Rh_{18}B_8$ [28], as well as in $Mg_{1-x}B_2$ [32]. In accordance with the electronegativities of the elements, magnesium carries the largest positive and iridium the largest negative charges (similar for the three positions), while the boron atoms show intermediate charges around zero. The relatively large charge difference between the boron sites may be understood considering their coordination. While the slightly positively charged B1 is surrounded by five electronegative iridium and two electropositive magnesium atoms, the B2 site is four-coordinated by Ir and has 2+6 magnesium atoms around the tetrahedron. The B2 species can better compensate the charge transferred to the more electronegative iridium atom and carry a small charge close to zero (–0.06 from LMTO-ASA and +0.06 from FPLO calculations). In general, charge transfer plays an important role in the organization of the crystal structure of $Mg_{10}Ir_{19}B_{16}$.

Distribution of the electron localizability indicator in $Mg_{10}Ir_{19}B_{16}$ reveals maxima of ELI-D between B and Ir (Fig. 5), visualizing direct covalent bonding within the B–Ir framework. Despite the visual perception of the maximum of ELI-D along the B–Ir contacts to be located closer to the boron nucleus, detailed analysis applying the ELI-D/electron density intersection technique shows that the major part of the bonding ELI-D basin is located within the atomic basin of iridium, confirming the polar character of the B–Ir covalent interaction, as expected from the QTAIM charges and the electronegativities of B and Ir. Additionally, this is supported by the structuring of the penultimate shells of part of the Ir atoms

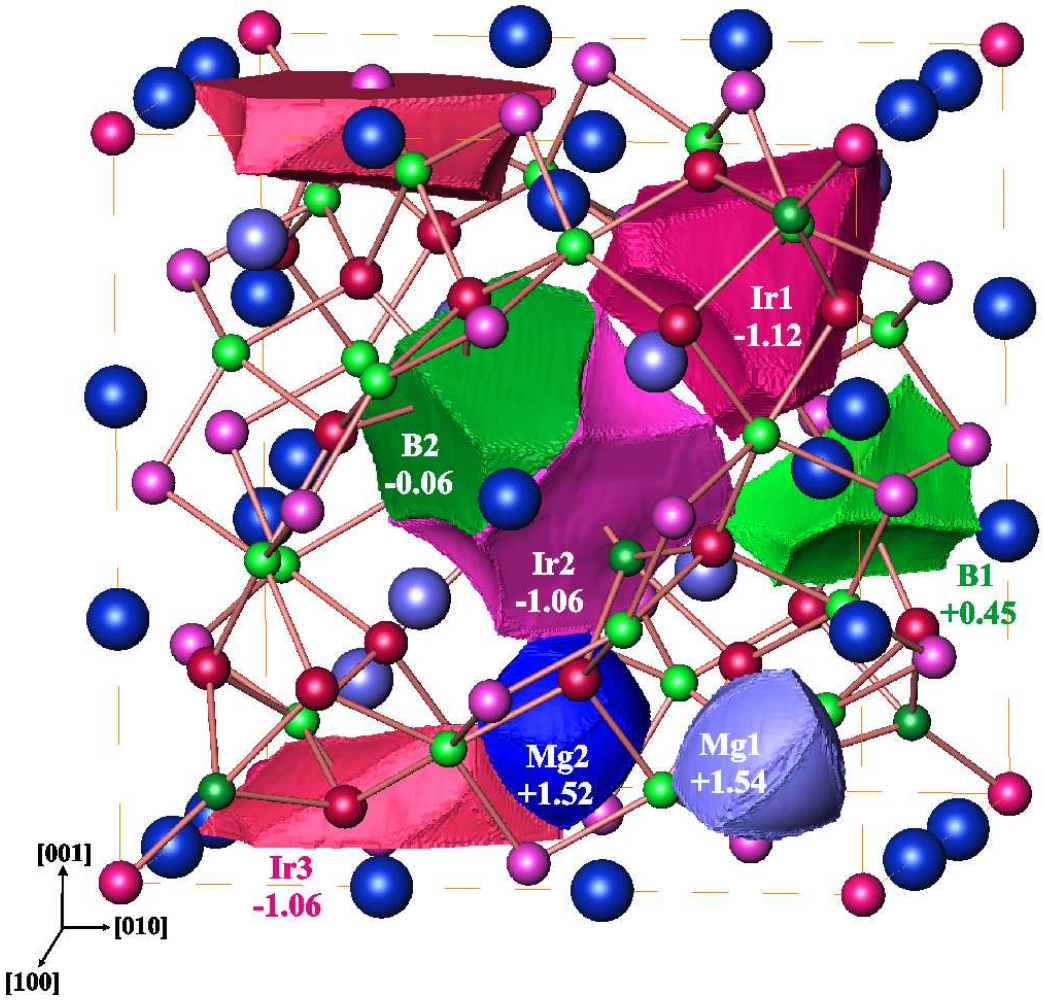


**Fig. 4** QTAIM atomic basins and effective charges in $Mg_{10}Ir_{19}B_{16}$.

(Fig. 5, top), which is a fingerprint of the participation of the electrons of these shells in the bonding within the valence region [21,33], in agreement with the split of the *d* states in the electron DOS (Fig. 3). The structuring is markedly pronounced for Ir1 and Ir2, but less recognizable for Ir3. Most of the bonding B–Ir ELI-D basins are disynaptic, *i.e.* have common faces only with two according core basins of Ir and B, visualizing two-center interactions (Fig. 5, bottom left and right). Solely around the five-coordinated B1, the maxima of ELI-D are located in triangles Ir3–B1–Ir3 resembling a three-center interaction (Fig. 5, bottom middle).

The ELI-D distribution in the penultimate shells of the Mg species is spherical. The Mg species are well separated from the environment by regions with small ELI-D values (Fig. 5, top and middle). These features support the expected cationic character of Mg, in good agreement with the QTAIM charges. Slightly unexpectedly, additional ELI-D maxima are observed along the Mg1–Ir3 and Mg2–Ir1 contacts (marked by black circles in Fig. 5, top and middle), similar to those recently found between Ba and Au in $Ba_8Au_6Ge_{40}$ [34] indicating a dative interaction between Ir and Mg, in addition to the ionic one. This feature is not affected by the method of calculation; the LMTO-ASA and FPLO calculations differ only in the local topology of ELI in the regions of Mg–Ir interactions. From the FPLO calculations, the Mg1–Ir3 interaction is revealed by a clear ELI maximum, whereas in the Mg2–Ir1 region, only a strong distortion of the ELI distribution is observed.

The atomic interactions in $Mg_{10}Ir_{19}B_{16}$ can be summarized as follows: the framework is formed by covalent polar B–Ir bonds. Formation of such an anionic covalently-bonded substructure of platinum metal and boron is also known for other ternary

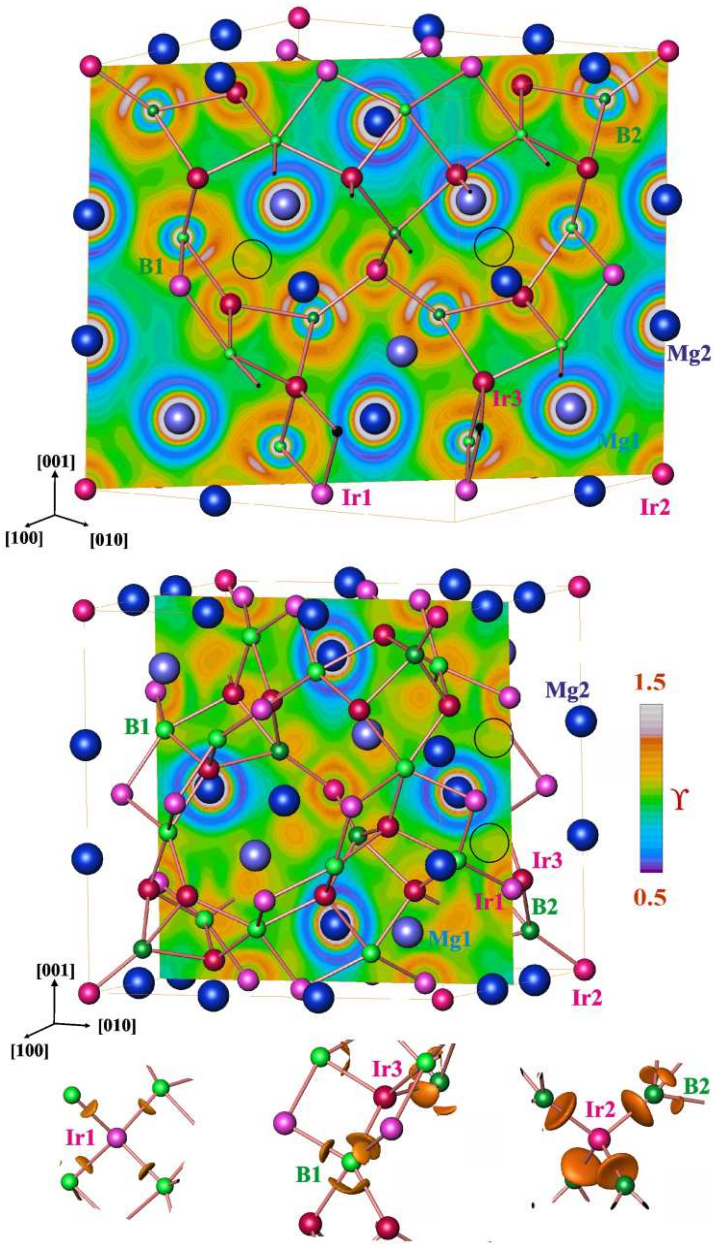


**Fig. 5** Electron localizability indicator in $Mg_{10}Ir_{19}B_{16}$: (top) ELI-D distribution in the (110) plane; (middle) ELI-D distribution in the (200) plane; (bottom) isosurfaces with $\Upsilon = 1.23$ visualizing the interaction in the environments of Ir1 (left), B1 and Ir3 (middle), Ir2 and B2 atoms (right); small black circles indicate the Mg–Ir interactions.

magnesium-platinum metal borides [28,35]. Mainly ionic interactions were found between the Mg cations and the framework, supported by additional dative Ir–Mg bonding. A previous description of the structure of $Mg_{10}Ir_{19}B_{16}$, given in [9], was based on a direct comparison of the metal-metal contact lengths, Ir–Ir and Mg–Mg, with those in the elemental metals. The presence of short (~2.71 Å) Ir–Ir distances suggests the existence of an Ir-only based framework. The Mg-substructure was described in a similar manner. The proposed structure description (an onion-skin-like series of nested polyhedra) suggests negligible interaction between the substructures. This description was not supported by the present analysis of the chemical bonding, using quantum-chemical tools.

The tetrahedral environment of all but the B1 atoms in the framework suggests a Zintl-like

mechanism of chemical bonding in the title compound. The corresponding electron balance can be formulated with two assumptions. The first one is the hypothetic tetrahedral coordination of all the boron and iridium atoms, including B1. The second one takes into account ELI-D topology features, namely the weaker structuring of the penultimate shell of the Ir3 atoms in comparison with the Ir1 and Ir2 atoms. This can be interpreted as the transfer of two *d* electrons to the outer valence shell of the Ir1 and Ir2 atoms, but only one for the Ir3 atoms. In this case the Ir1 and Ir2 atoms do not need additional electrons to form four 2*c*2*e*-bonds, but the Ir3 atom has to accept one electron to achieve tetrahedral coordination. However, the corresponding electron balance is strongly electron deficient: $[Mg^{2+}]_{10}[(4b)Ir1^{0}]_{6}[(4b)Ir2^{0}]_{1}[(4b)Ir3^{1-}]_{12}[(4b)B1^{1-}]_{12}[(4b)B2^{1-}]_{4}*8p^{1+}$.

The picture presented above is in agreement with the pseudo gap in the electronic DOS, located above the Fermi level. Integration of the DOS in the region between $E_F$ and +1.2 eV yields seven holes. This feature is less pronounced in the FPLO calculations (pseudo gap at +0.73 eV), giving five holes. This deficiency is resolved by formation of three-center Ir3–B1–Ir3 interactions, leading to a charge-balanced situation: $[Mg^{2+}]_{10}[(4b)Ir1^{0}]_{6}[(4b)Ir2^{0}]_{1}[(4b)Ir3^{0.67-}]_{12}[(5b)B1^{0.67-}]_{12}[(4b)B2^{1-}]_{4}$.

On the other hand, this electron instability may be one of the reasons for the appearance of the superconducting state at low temperatures, similarly to the situation found for magnesium diboride.

*5. Physical properties measurements*

The results of the physical properties measurements performed on the samples of $Mg_{10}Ir_{19}B_{16}$ prepared in this study are similar to those presented earlier [5,10]. Studies of the magnetic susceptibility $\chi = M/H$ in various fields revealed ferromagnetic and Curie-paramagnetic impurities in/on the sample, hampering a closer analysis. The estimated value of the intrinsic susceptibility is $\chi_0 = -0.3(1)\times10^{-3}$ emu mol$^{-1}$, indicating prevailing diamagnetism of the compound.

In low magnetic fields, the compound undergoes a superconducting transition at $T_c = 4.2$ K. A sample with a large amount of competing phases did not show a significantly different $T_c$, in agreement with the point composition of the $Mg_{10}Ir_{19}B_{16}$ phase (*cf.* lattice parameter study above, Table 5). After zero-field cooling (zfc) to 1.8 K, the volume magnetic susceptibility in a field of ≈ 10 Oe is well in excess of $-1/4\pi$, which is due to the large demagnetization factor of the platelet-shaped sample perpendicular to the direction of the applied field. The flux expulsion measured during field cooling (fc) is dramatically less (only $0.18 \times -1/4\pi$), which is probably due to strong flux line pinning in this type II superconductor [10]. The superconducting signal disappeared in the 10 kOe data (*i.e.* $T_c < 1.8$ K), in agreement with critical field data [10].

Resistivity measurements with a current density of 2.4 A mm$^{-2}$ showed onset of the superconducting transition at $T_c = 4.2$ K and zero resistance at 4.0 K. Above $T_c$, the sample revealed a typical metallic temperature dependence of the resistivity ($\rho_{300\,K}$ = 8 μΩ m; residual resistivity ratio ≈ 9). The increase of the resistivity in a magnetic field of 90 kOe compared to zero field at temperatures just above $T_c$ is +3 %. Such a small value is also typical for a non-magnetic intermetallic compound.

## Conclusions

The crystal structure of $Mg_{10}Ir_{19}B_{16}$, determined from single crystal X-ray diffraction data, is well ordered and does not show detectable vacancies. The lattice parameter does not vary in multi-phase samples of different compositions, indicating constant composition of the phase. Analysis of the chemical bonding by the electron localizability approach revealed a three-dimensional covalently bonded anionic B–Ir framework. In addition to the ionic bonding of magnesium with the framework, dative Mg–Ir interactions were found.

## Acknowledgements

The authors thank Dr. Gudrun Auffermann and Mrs. Ulrike Schmidt for the chemical analyses. Dr. Ulrich Burkhardt is acknowledged for support in the metallographic studies; Dr. Reiner Ramlau and Mrs. Katja Schulze are thanked for the EDXS and WDXS measurements. A.A.M. and E.V.A acknowledge (partial) support from the Program of Development of Lomonosov Moscow State University.

## References

[1] J. Nagamatsu, N. Nakagawa, T. Muranaka, Y. Zenitani, J. Akimitsu, *Nature* 410 (2001) 63-64.
[2] C. Buzea, T. Yamashita, *Supercond. Sci. Technol.* 14 (2001) R115-R146.
[3] T. Muranaka, J. Akimitsu, *Z. Kristallogr.* 226 (2011) 385-394.
[4] R.J. Cava, H.W. Zandbergen, K. Inumaru, *Physica C* 385 (2003) 8-15.
[5] T. Klimczuk, Q. Xu, E. Morosan, J.D. Thompson, H.W. Zandbergen, R.J. Cava, *Phys. Rev. B* 74 (2006) 220502.
[6] G. Mu, Y. Wang, L. Shan, H.-H. Wen, *Phys. Rev. B* 76 (2007) 064527.
[7] K. Tahara, Z. Li, H.X. Yang, J.L. Luo, S. Kawasaki, G.-q. Zheng, *Phys. Rev. B* 80 (2009) 060503.

[8] G. Mu, H. Yang, H.-H. Wen, *Phys. Rev. B* 76 (2010) 052501.
[9] Q. Xu, T. Klimczuk, T. Gortenmulder, J. Jansen, M.A. McGuire, R.J. Cava, H.W. Zandbergen, *Chem. Mater*. 21 (2009) 2499-2507.
[10] T. Klimczuk, F. Ronning, V. Sidorov, R.J. Cava, J.D. Thompson, *Phys. Rev. Lett.* 99 (2007) 257004.
[11] I. Bonalde, R.L. Ribeiro, W. Brämer-Escamilla, G. Mu, H.-H. Wen, *Phys. Rev. B* 79 (2009) 052506.
[12] A.A. Aczel, T.J. Williams, T. Goko, J.P. Carlo, W. Yu, Y.J. Uemura, T. Klimczuk, J.D. Thompson, R.J. Cava, G.M. Luke, *Phys. Rev. B* 82 (2010) 024520.
[13] STOE WinXPOW, Version 1.2, STOE & Cie GmbH, Darmstadt, Germany, 2000.
[14] W. Schnelle, U. Burkhardt, R. Ramlau, R. Niewa, G. Sparn, *Sci. Rep. 2001/2002, Max-Planck-Institut für Chemische Physik fester Stoffe*, Dresden, Germany, 2003, pp. 38-43.
[15] S.M. Seltzer, *Radiat. Res.* 136 (1993) 147-170.
[16] L.G. Akselrud, Yu. Grin, *J. Appl. Crystallogr*. 47 (2014) 803-805.
[17] O. Jepsen, A. Burkhardt, O.K. Andersen, *The Program TB-LMTO-ASA, 4.7*; Max-Planck-Institut für Festkörperforschung, Stuttgart, 1999.
[18] U. von Barth, L. Hedin, *J. Phys. C* 5 (1972) 1629-1642.
[19] O.K. Andersen, *Phys. Rev. B* 12 (1975) 3060-3083.
[20] M. Kohout, *Int. J. Quantum Chem*. 97 (2004) 651-658.
[21] F.R. Wagner, V. Bezugly, M. Kohout, Yu. Grin, *Chem. Eur. J*. 13 (2007) 5724-5741.
[22] M. Kohout, *Faraday Discuss*. 135 (2007) 43–54.
[23] R.F.W. Bader, *Atoms in Molecules, A Quantum Theory*, Clarendon Press and Oxford University Press Inc., New York, 1994.
[24] M. Kohout, *DGrid, version 4.6*, Radebeul, Germany, 2011.
[25] Inorganic Crystal Structure Database (ICSD), Fachinformationszentrum Karlsruhe, Germany, Version 2012-1.
[26] J. Emsley, *The Elements*, Oxford University Press Inc., New York, 1991.
[27] A.M. Alekseeva, A.M. Abakumov, P.S. Chizhov, A. Leithe-Jasper, W. Schnelle, Yu. Prots, J. Hadermann, E.V. Antipov, Yu. Grin, *Inorg. Chem*. 46 (2007) 7378-7286.
[28] A.M. Alekseeva, A.M. Abakumov, A. Leithe-Jasper, W. Schnelle, Yu. Prots, G. Van Tendeloo, E.V. Antipov, Yu. Grin, *Chem. Eur. J*. 19 (2013) 17860-17870.
[29] B. Wiendlocha, J. Tobola, S. Kaprzyk, arXiv:0704.1295v1 [cond-mat.supr-con] 10 April 2007.
[30] M. Samsel-Czekala, M.J. Winiarski, *Intermetallics* 31 (2012) 186-190.
[31] J.H. Roudebush, N. Tsujii, A. Hurtando, H. Hope, Yu. Grin, S. Kauzlarich, *Inorg. Chem*. 51 (2012) 4161-4169.
[32] V. Tsirelson, A. Stash, M. Kohout, H. Rosner, H. Mori, S. Sato, S. Lee, A. Yamamoto, S. Tajima, Yu. Grin, *Acta Crystallogr. B* 59 (2003) 575-583.
[33] M. Kohout, F.R. Wagner, Yu. Grin, *Theor. Chem. Acc*. 108 (2002) 150-156.
[34] H. Zhang, H. Borrmann, N. Oeschler, C. Candolfi, W. Schnelle, M. Schmidt, U. Burkhardt, M. Baitinger, J.-T. Zhao, Yu. Grin, *Inorg. Chem*. 50 (2011) 1250-1257.
[35] A.M. Alekseeva, A.M. Abakumov, A. Leithe-Jasper, W. Schnelle, Yu. Prots, J. Hadermann, G. Van Tendeloo, E.V. Antipov, Yu. Grin, *Z. Anorg. Allg. Chem.* 631 (2005) 1047-1054.